



Left-right splitting of elliptic flow due to directed flow in heavy ion collisions

Chao Zhang ^{1,2} and Zi-Wei Lin ^{1,*}

¹*Department of Physics, East Carolina University, Greenville, North Carolina 27858, USA*

²*Institute of Particle Physics and Key Laboratory of Quark & Lepton Physics (MOE), Central China Normal University, Wuhan 430079, China*



(Received 10 September 2021; revised 14 August 2022; accepted 16 November 2022; published 30 November 2022)

Recently the splitting of elliptic flow v_2 at finite rapidities has been proposed as a result of the global vorticity in noncentral relativistic heavy ion collisions. In this study, we find that this left-right (i.e., on opposite sides of the impact parameter axis) splitting of the elliptic flow at finite rapidities is a result of the nonzero directed flow v_1 , with the splitting magnitude $\approx 8v_1(1 - 3v_2)/(3\pi)$. We also use a multiphase transport model, which automatically includes the vorticity field and flow fluctuations, to confirm the v_2 splitting. In addition, we find that the analytical expectations for the v_2 splitting work for the raw v_2 and v_1 (i.e., before event plane resolutions are applied) measured relative to either the first- or second-order event plane. Since the v_2 splitting is mostly driven by v_1 , it vanishes at zero transverse momentum (p_T), and its magnitude and sign may have nontrivial dependencies on p_T , centrality, collision energy, and hadron species.

DOI: [10.1103/PhysRevC.106.054910](https://doi.org/10.1103/PhysRevC.106.054910)

I. INTRODUCTION

Heavy ion collisions provide us a way to study the properties of the created matter in relation to the theory of quantum chromodynamics. At high-enough energies, the created matter should be initially deconfined and be represented by parton degrees of matter, the quark-gluon plasma (QGP) [1]. Anisotropic flows in the final particle momentum distribution are powerful tools to study heavy ion physics [2]. They include the directed flow v_1 , elliptic flow v_2 , the more recently discovered triangular flow v_3 [3], and higher-order flows. Significant anisotropic flows have been observed in noncentral heavy ion collisions [4–6], while they have also been observed in small systems such as $p + \text{Au}$, $d + \text{Au}$, $\text{He} + \text{Au}$ [7], and $p + \text{Pb}$ [8] collisions at high energies. It is well known that the initial geometry of the overlap volume in a heavy ion collision has a fluctuating and complicated event-by-event three-dimensional structure, and the initial spatial anisotropies are converted into anisotropic flows in momentum through particle interactions in transport models or the pressure gradient in hydrodynamical models. On the other hand, the origin of flowlike behavior in small systems including $p + p$ collisions is still under debate, where initial-state correlations [9,10], the parton escape mechanism [11,12] or kinetic theory [13,14], and hydrodynamics [15,16] have been proposed as the dominant mechanism.

Recently, the splitting of elliptic flow on opposite sides of the impact parameter axis has been proposed as a new observable [17], where it is argued to be the result of the global vorticity in noncentral relativistic heavy ion collisions.

In this study, we examine this v_2 splitting in A + A collisions at RHIC and LHC energies.

II. METHOD

After a brief analysis of the left-right v_2 splitting that relates it to v_1 , we shall use a multiphase transport (AMPT) model [18,19] to test the relationship. The AMPT model is an event generator for relativistic heavy ion collisions that contains four parts: the fluctuating initial condition based on the HIJING model, the parton cascade model ZPC for elastic scatterings, a spatial quark coalescence model to describe the hadronization, and a hadron cascade. The string melting version of the AMPT model [18,20] is applicable at high energies when the QGP is expected to be formed. It has been shown to well describe the bulk matter including the overall elliptic flow [20,21] and the vorticity field [22,23] in heavy ion collisions. Its fluctuating initial condition also creates spatial anisotropies that lead to anisotropic flows of different orders [3]. Recently we have updated the AMPT model with a new quark coalescence model [24], modern parton distribution functions in nuclei [25], and improved heavy quark productions [26]. In addition, we have applied local nuclear scaling to two key parameters in the AMPT initial condition, which enables the model to self-consistently describe the system size and centrality dependence of nuclear collisions [19]. For this study, we employ the string melting version of the AMPT model that contains the above improvements.

In the AMPT model [18], the x axis is along the impact parameter (\vec{b}) in the transverse plane of each event, where the centers of the projectile and target nuclei are at the transverse position $(b/2, 0)$ and $(-b/2, 0)$, respectively. The direction of the projectile momentum specifies the z axis; as a result, the total angular momentum of the system is along the

*linz@ecu.edu

– y direction [22]. Note that this coordinate system is the same as that in the recent study that first proposed the v_2 splitting [17]. In Sec. III, we analyze the v_2 splitting and calculate flows using the theoretical reaction plane for simplicity. Then in Sec. IV we use the experimental event plane method to calculate the flows and v_2 splitting.

III. RESULTS USING THE REACTION PLANE

Let us write the normalized azimuthal distribution in momentum for particles in a given phase space, e.g., at a given p_T and rapidity y or pseudorapidity η , as

$$f(\phi) = \frac{1}{2\pi} \left(1 + \sum_{n=1}^{\infty} [c_n \cos(n\phi) + s_n \sin(n\phi)] \right). \quad (1)$$

The above gives the usual relations $\langle \cos \phi \rangle = c_1/2 \equiv v_1$ and $\langle \cos(2\phi) \rangle = c_2/2 \equiv v_2$ when we integrate over the full range of ϕ in the averaging over particles and events. On the other hand, if we integrate over $\phi \in (-\pi/2, \pi/2)$ for the $p_x > 0$ part or over $\phi \in (\pi/2, 3\pi/2)$ for the $p_x < 0$ part, we obtain the following for v_2 (with terms up to $n = 4$):

$$v_2(p_x > 0) \equiv \frac{\int_{-\pi/2}^{\pi/2} \cos(2\phi) f(\phi) d\phi}{\int_{-\pi/2}^{\pi/2} f(\phi) d\phi} = \frac{v_2 + \frac{4v_1}{3\pi} + \frac{6c_3}{5\pi}}{1 + \frac{4v_1}{\pi} - \frac{2c_3}{3\pi}},$$

$$v_2(p_x < 0) \equiv \frac{\int_{\pi/2}^{3\pi/2} \cos(2\phi) f(\phi) d\phi}{\int_{\pi/2}^{3\pi/2} f(\phi) d\phi} = \frac{v_2 - \frac{4v_1}{3\pi} - \frac{6c_3}{5\pi}}{1 - \frac{4v_1}{\pi} + \frac{2c_3}{3\pi}}. \quad (2)$$

Note that the coefficient $c_3 = 2\langle \cos(3\phi) \rangle$ does not correspond to (twice) the usual triangular flow v_3 [3], which axes fluctuate mostly independently of the x axis (or the reaction plane). Instead, c_3 here is calculated relative to the reaction plane and represents another type of triangular flow at finite rapidities that correlates with the reaction plane, and it is expected to be rapidity-odd. If $|c_3| \ll |v_1|$, we can neglect c_3 and get simpler relations (up to second order in v_1 and/or v_2):

$$v_2(p_x > 0) \simeq \frac{v_2 + \frac{4v_1}{3\pi}}{1 + \frac{4v_1}{\pi}} \simeq v_2 - \frac{16v_1^2}{3\pi^2} + \frac{4v_1}{3\pi}(1 - 3v_2),$$

$$v_2(p_x < 0) \simeq \frac{v_2 - \frac{4v_1}{3\pi}}{1 - \frac{4v_1}{\pi}} \simeq v_2 - \frac{16v_1^2}{3\pi^2} - \frac{4v_1}{3\pi}(1 - 3v_2). \quad (3)$$

Therefore, the left-right v_2 splitting at finite rapidities, given by $v_2(p_x > 0) - v_2(p_x < 0) \simeq 8v_1(1 - 3v_2)/(3\pi)$, comes directly from the finite directed flow v_1 .

We now use the AMPT model to test these relationships. Figure 1 shows the results of $v_2(p_T)$ of charged hadrons and final state partons with $p_x > 0$, $p_x < 0$, and all p_x for minimum bias Au + Au collisions at 200A GeV. Results for the pseudorapidity ranges of $0 < \eta < 2$ and $-2 < \eta < 0$ are shown in the left and right panels, respectively. We see that the left-right splitting of elliptic flow exists for both partons and hadrons in the final state. The v_2 splitting is small at low p_T and then become obvious for partons at $p_T > 1$ GeV/c and for hadrons at $p_T > 1.5$ GeV/c. In addition, we see that the v_2 splitting is antisymmetric versus η , which is mostly due to the rapidity-odd v_1 as $c_3 \simeq 0$ in this figure. Note that we call this the left-right splitting of the elliptic flow v_2 , because

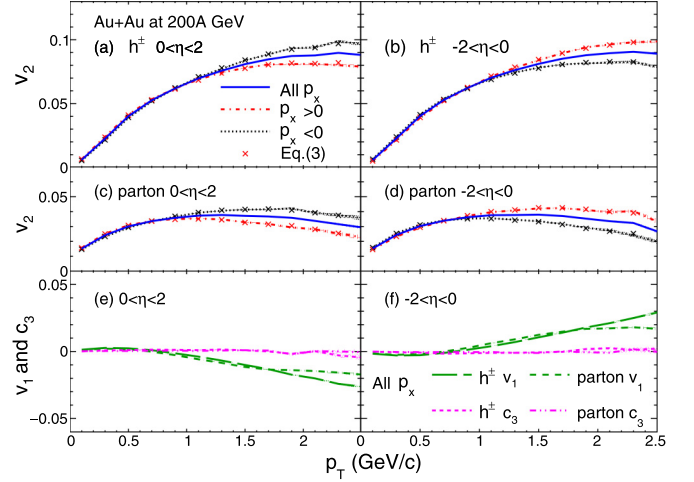


FIG. 1. Left panels show (a) v_2 of charged hadrons, (c) v_2 of partons, (e) v_1 and c_3 within $0 < \eta < 2$ versus the transverse momentum for minimum bias Au + Au collisions at 200A GeV from the AMPT model. The overall v_2 (solid), $v_2(p_x > 0)$ (dot-dashed), and $v_2(p_x < 0)$ (dotted) are shown, while crosses represent the expectations of Eq. (3). The corresponding results for particles within $-2 < \eta < 0$ are shown in the right panels.

particles with $p_x > 0$ and $p_x < 0$ are on the right and left side of the impact parameter axis, respectively. This also helps to differentiate it from the v_2 splitting between particles and antiparticles, which has been shown to be sensitive to partonic and hadronic potentials at low energies or high net-baryon chemical potential [27,28].

We also show in Figs. 1(e) and 1(f) the overall $v_1(p_T)$ of charged hadrons and partons at positive and negative pseudorapidities, respectively. The expectations from Eq. (3) using the overall (i.e., all p_x) $v_1(p_T)$ and $v_2(p_T)$ are shown by the cross symbols in Figs. 1(a)–1(d), which agree well with the directly calculated v_2 splitting curves. The good agreements with Eq. (3) in Fig. 1 also indicate $c_3(p_T) \simeq 0$ there, which we confirm in Figs. 1(e) and 1(f) with direct calculations of $c_3(p_T)$ (magenta curves).

Next we investigate the possible centrality dependence of the v_2 splitting in Fig. 2, which shows the AMPT results of $v_2(p_T)$ for charged hadrons within $0 < \eta < 2$ for different centralities of Au + Au collisions at 200A GeV. Here centrality is determined with the charged hadron multiplicity within mid-pseudorapidity. We observe the v_2 splitting at all centralities (except for very peripheral collisions where the statistical errors are relatively large). In addition, the order of the splitting at higher p_T , i.e., the sign of $v_2(p_x > 0) - v_2(p_x < 0)$, does not change with centrality here. It is also interesting to see that the v_2 splitting exists even in the most central (0%–5%) events.

Figure 3 shows the centrality dependence of the integrated v_2 of charged hadrons with positive or negative p_x in Au + Au collisions at 200A GeV from the AMPT model. The v_2 integrated over $p_T > 1.5$ GeV/c shows a significant left-right splitting, consistent with that shown in Fig. 2. On the other hand, the v_2 integrated over all p_T shows a very small splitting, while the order of splitting is also opposite to that

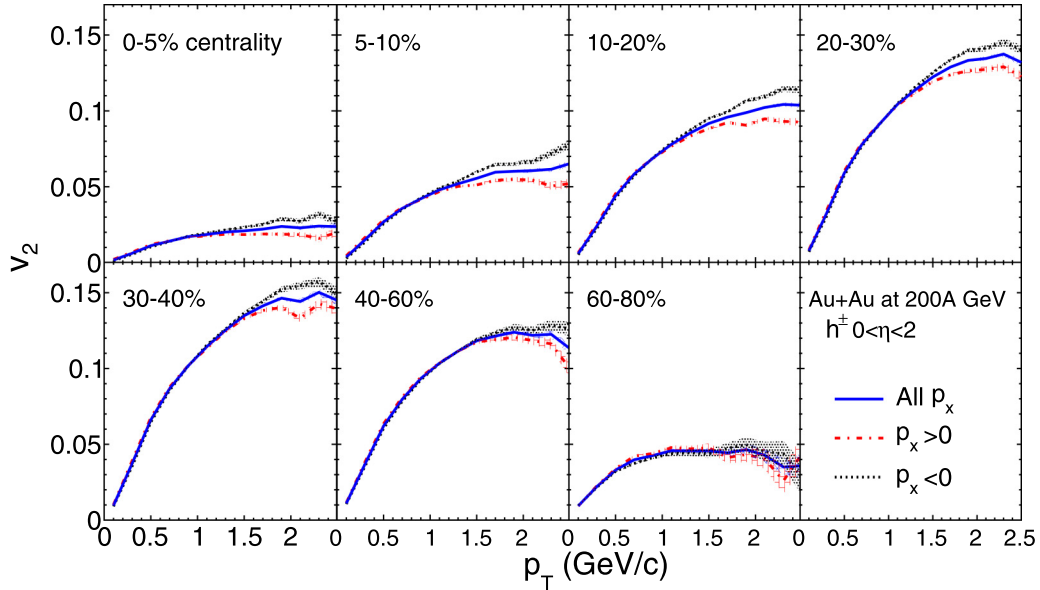


FIG. 2. The overall and split $v_2(p_T)$ of charged hadrons within $0 < \eta < 2$ for different centralities of Au + Au collisions at 200A GeV from the AMPT model.

of the v_2 integrated over $p_T > 1.5$ GeV/c. This is because the directed flow v_1 from the AMPT model changes sign at $p_T \sim 0.7$ GeV/c, as shown in Fig. 1. We also show in Fig. 3 the ratio $v_2(p_x > 0)/v_2(p_x < 0)$ to represent the relative left-right v_2 splitting. While the ratio of the split v_2 integrated over all p_T is rather flat versus centrality, the ratio of the split v_2 integrated over $p_T > 1.5$ GeV/c shows a significant dependence on centrality, where the relative splitting is the biggest for the most central events. This is possible because, although both v_2 and v_1 usually approach zero for central collisions, the relative v_2 splitting mostly depends on v_1/v_2 , which could be large.

In Fig. 4 we examine the v_2 splitting at different energies at RHIC and LHC, where the upper panels [(a)–(c)] show the AMPT $v_2(p_T)$ results of charged hadrons within $0 < \eta < 2$

in minimum bias Au + Au collisions at 11.5A and 200A GeV and minimum bias Pb + Pb collisions at 5.02A TeV. The magnitude of the v_2 splitting decreases as the colliding energy increases; this is expected because the directed flow v_1 is usually smaller at higher energies. We also see that the order of splitting can be different at different energies as a result of the sign of $v_1(p_T)$. The expectations from Eq. (3), shown as the cross symbols, agree rather well with the split v_2 results at all three energies, although there is a small discrepancy at 11.5A GeV. This discrepancy is due to the c_3 terms in Eq. (2), because c_3 is not very small at 11.5A GeV as shown in Fig. 4(a). In cases where $|c_3| \ll |v_1|$ is not true, Eq. (3) is not accurate enough while Eq. (2) still is. In the lower panels of Fig. 4, we show the split $v_2(p_T)$ results for charged hadrons within $0 < \eta < y_{\text{beam}}$, where y_{beam} is the projectile rapidity in the center-of-mass frame of the heavy ion collision. We see that the magnitudes of the v_2 splitting are similar at these different energies, and the wider η range increases the magnitude of v_2 splitting at high energies due to the big v_1 magnitudes at large rapidities. This suggests that the left-right v_2 splitting could be observed even at LHC energies if one looks at large rapidities.

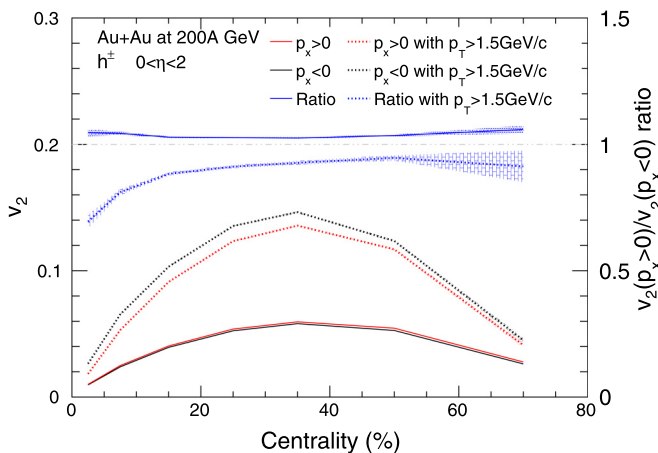


FIG. 3. Centrality dependence of p_T -integrated v_2 for charged hadrons with positive or negative p_x and their ratio (blue curves). Solid and dotted v_2 curves represent the results integrated over all p_T and over $p_T > 1.5$ GeV/c, respectively.

IV. RESULTS USING THE EVENT PLANE

So far we have used the theoretical reaction plane (RP) for the flow analysis. We now use the experimental event plane method to see whether the v_2 splitting can be observed experimentally. Specifically, we use minimum bias Au + Au collisions at 11.5A GeV as the example. The event plane angle Ψ_n is calculated with the event-by-event flow vector \vec{Q}_n [29,30] according to

$$X_n = \sum_i w_i \cos(n\phi_i), \quad Y_n = \sum_i w_i \sin(n\phi_i),$$

$$\Psi_n = \arctan2(Y_n, X_n)/n. \quad (4)$$

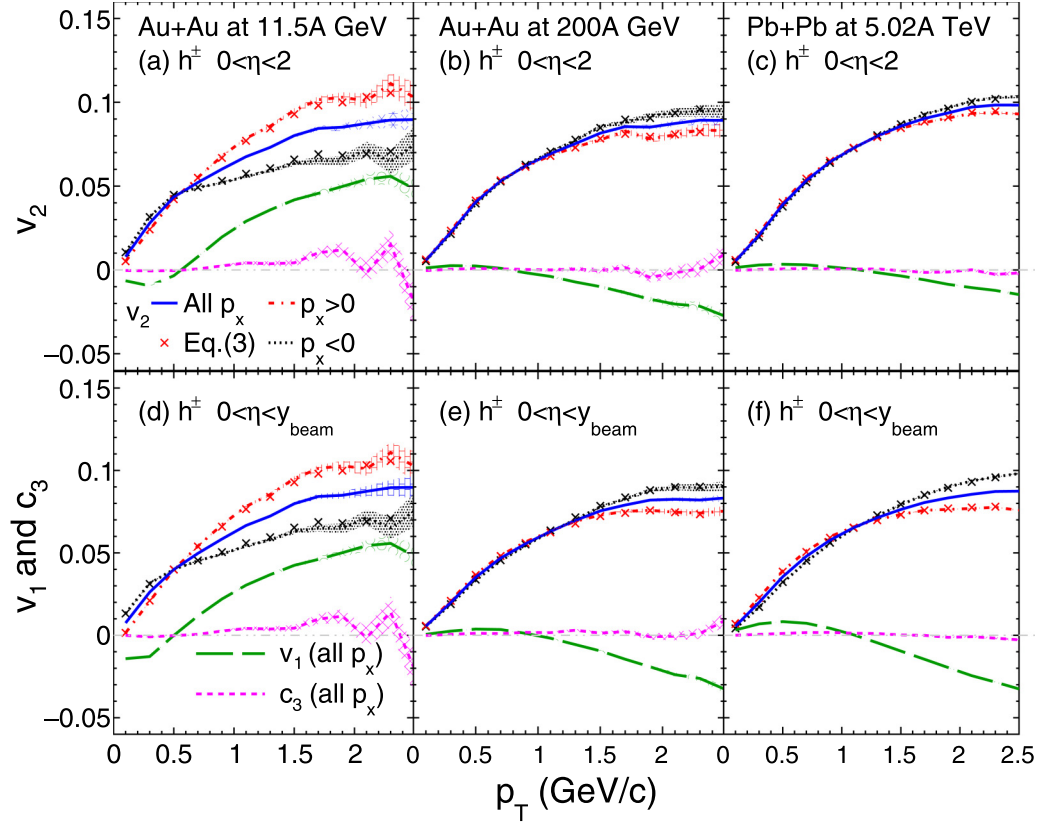


FIG. 4. The overall v_2 (solid), $v_2(p_x > 0)$ (dot-dashed), $v_2(p_x < 0)$ (dotted), v_1 (long-dashed), and c_3 (dashed) of charged hadrons within $0 < \eta < 2$ in minimum bias (a) Au + Au collisions at 11.5A, (b) 200A GeV and (c) Pb + Pb collisions at 5.02A TeV. The corresponding results within $0 < \eta < y_{\text{beam}}$ are shown in the lower panels, while crosses represent the expectations of Eq. (3).

In the above, ϕ_i is the azimuthal angle of the i th particle's momentum in the event, and the weight w_i is taken as the particle transverse momentum. The first-order event plane angle Ψ_1 is reconstructed from two flow vectors: $\vec{Q}_{1,\text{west}}$ from $3.5 < \eta < 5.09$ and $\vec{Q}_{1,\text{east}}$ from $-5.09 < \eta < -3.5$. The first-order flow vector of the full event is then reconstructed as $\vec{Q}_1 = \vec{Q}_{1,\text{west}} - \vec{Q}_{1,\text{east}}$. Note that we have chosen a narrower η range than the STAR event plane detector (EPD) system [31] to get a better resolution of Ψ_1 . The second-order event plane angle Ψ_2 is reconstructed from the flow vector of particles within $-2 < \eta < 2$.

A. Relative to the first-order event plane Ψ_1

Flow coefficients relative to the first-order event plane are calculated as

$$v_n\{\Psi_1\} \equiv \frac{v_n^{\text{obs}}}{R_n\{\Psi_1\}} = \frac{\langle\langle \cos[n(\phi - \Psi_1)] \rangle\rangle}{\langle \cos[n(\Psi_1 - \Psi_r)] \rangle}. \quad (5)$$

In the above, Ψ_r represents the ‘‘true’’ reaction plane angle, and the numerator represents the observed (or raw) anisotropic flows which are directly measured in the experiments, where the double brackets represent the averaging over particles in each event and then over all events. The denominator represents the event plane resolution, where the single bracket represents the averaging over all events. We follow the two-subevent method [29] to

calculate the resolutions, where the two subevents are from $3.5 < \eta < 5.09$ and $-5.09 < \eta < -3.5$, respectively, for calculating $R_n\{\Psi_1\}$. Note that we use a modified equation $R_{2k+1}^{\text{sub}}\{\Psi_1\} = \sqrt{\langle \cos[(2k+1)(\Psi_1^a - \Psi_1^b - \pi)] \rangle}$ instead of $\sqrt{\langle \cos[(2k+1)(\Psi_1^a - \Psi_1^b)] \rangle}$ [29] to calculate the subevent resolution for the odd-order anisotropies, because $\Psi_{1,\text{west}}$ for one subevent is expected to be different from $\Psi_{1,\text{east}}$ for the other subevent by π on average. We then determine the χ_n^{sub} value from R_n^{sub} . Using $\chi_n = \sqrt{2}\chi_n^{\text{sub}}$ for the full event [29], we then obtain the full event resolutions $R_n\{\Psi_1\}$.

We show in Fig. 5 the v_2 splitting results relative to the first-order event plane after applying the resolution corrections with $R_n\{\Psi_1\}$. Note that here we treat the Ψ_1 angle as the x axis, where any hadron with $\cos(\phi - \Psi_1) > 0$ belongs to the $p_x > 0$ group. The upper two panels show the overall, left-side and right-side v_2 of charged particles within $0 < \eta < 2$ and $-2 < \eta < 0$, respectively, while the corresponding v_1 and c_3 results are shown in the lower panels. The cross symbols in Fig. 5(a) are the expectations of the split v_2 by applying Eq. (3) to the overall v_2 in panel (a) and overall v_1 in panel (c). It is clear that the expectations of Eq. (3) fail here. Since c_3 is not too small here, we also apply Eq. (2) to the overall v_2 in panel (b), and overall v_1 and overall c_3 in panel (d) to obtain the plus symbols; they still fail to describe the split v_2 curves in panel (b). In addition, the long-dashed curves in Fig. 5 are

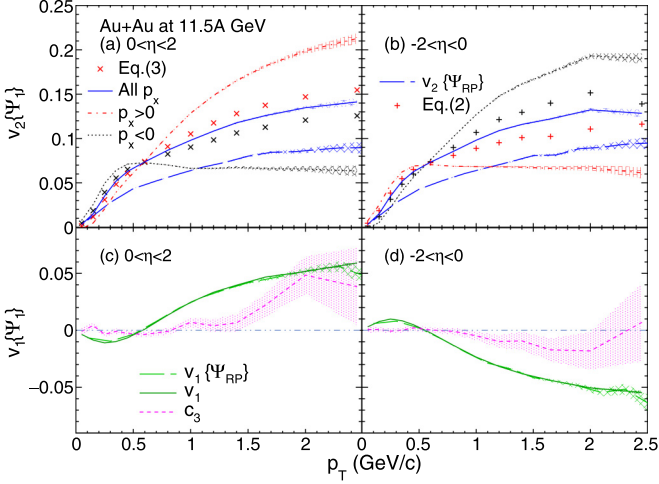


FIG. 5. (a) The overall and split v_2 , and (c) v_1 and c_3 of charged hadrons relative to the first-order event plane angle Ψ_1 versus the transverse momentum for $0 < \eta < 2$ in minimum bias Au + Au collisions at 11.5A GeV from the AMPT model. Results for $-2 < \eta < 0$ are shown in the right panels. Cross and plus symbols represent expectations of Eq. (3) and Eq. (2), respectively, and long-dashed curves represent v_2 (blue) and v_1 (green) relative to the theoretical reaction plane angle.

the $v_1\{\Psi_{RP}\}$ and $v_2\{\Psi_{RP}\}$ relative to the theoretical reaction plane, where $v_1\{\Psi_1\}$ well reproduces $v_1\{\Psi_{RP}\}$ while $v_2\{\Psi_1\}$ are different from $v_2\{\Psi_{RP}\}$.

The raw v_2 splitting results relative to the first-order event plane, i.e., without the resolution corrections, are shown in Fig. 6. We see in panel (a) that the split v_2 results (dot-dashed curve and dotted curve) agree well with the cross symbols, which are obtained by applying Eq. (3) to the overall v_1^{obs} and v_2^{obs} in the left panels. The split v_2 results in panel (b) also agree well with the plus symbols that are obtained by applying Eq. (2); this is expected since $c_3 \simeq 0$ in Fig. 6 and thus Eq. (2) and Eq. (3) are essentially the same. Therefore,

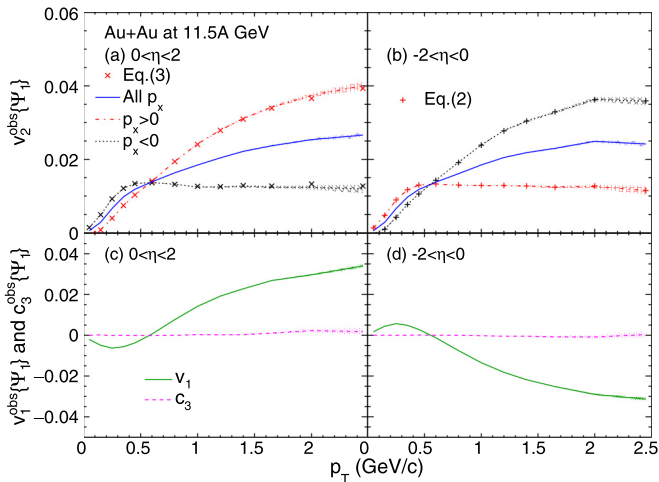


FIG. 6. Same as Fig. 5 but without the resolution corrections; here the v_2 splitting results agree with Eqs. (2) and (3).

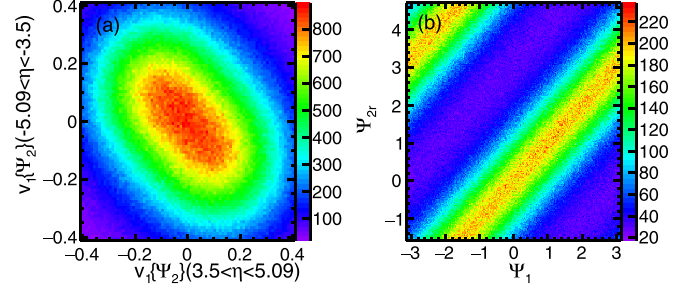


FIG. 7. AMPT results on the event-by-event (a) $v_1\{\Psi_2\}$ for particles within $-5.09 < \eta < -3.5$ versus that within $3.5 < \eta < 5.09$, and (b) reconstructed Ψ_{2r} versus Ψ_1 for minimum bias Au + Au collisions at 11.5A GeV.

the raw overall v_1 extracted with Eq. (3) from the split v_2 measurements relative to Ψ_1 can be corrected with its event plane resolution to yield the corrected v_1 , which will be equivalent to the standard $v_1\{\Psi_1\}$. It is also apparent that Eq. (2) and Eq. (3) fail in Fig. 5 because of the different resolution values for v_1 and v_2 . Specifically, $R_1\{\Psi_1\} = 0.574$, $R_2\{\Psi_1\} = 0.188$, and $R_3\{\Psi_1\} = 0.047$ are the resolutions used to obtain the corrected v_1 , v_2 , and c_3 in Fig. 5. In addition, it is interesting to see the large relative v_2 splitting in Fig. 6; this is mostly due to the higher resolution $R_1\{\Psi_1\}$ than $R_2\{\Psi_1\}$, which makes $v_1^{\text{obs}}/v_2^{\text{obs}}$ much bigger than the corrected v_1/v_2 .

B. Relative to the second-order event plane

Here we explore the v_2 splitting analysis relative to the second-order event plane. First, we need to know the second-order event plane angle that points toward the direction of the impact parameter, which we call Ψ_{2r} , to distinguish the left side from the right side. However, the standard Ψ_2 does not contain this information since $\Psi_2 \in (-\pi/2, \pi/2)$ has a range of π instead of 2π . We thus propose the following correlator for each event:

$$v_1\{\Psi_2\} = \langle \cos(\phi - \Psi_2) \rangle. \quad (6)$$

In the above, ϕ is the azimuthal angle of a particle within the narrowed EPD η range, Ψ_2 is the second-order event plane angle, and the bracket $\langle \rangle$ represents the averaging over particles in the event. We then use the sign of $v_{1,\text{west}}\{\Psi_2\}$ (for particles within the narrowed EPD range $3.5 < \eta < 5.09$) to determine the directional second-order event plane angle Ψ_{2r} :

$$\begin{aligned} \Psi_{2r} &= \Psi_2, & \text{if } v_{1,\text{west}}\{\Psi_2\} \geq 0, \\ &= \Psi_2 + \pi, & \text{otherwise.} \end{aligned} \quad (7)$$

For the v_2 splitting analysis, we treat the Ψ_{2r} angle as the x axis; e.g., any hadron with $\cos(\phi - \Psi_{2r}) > 0$ belongs to the $p_x > 0$ group.

Figure 7(a) shows the event-by-event correlation between $v_1\{\Psi_2\}$ from particles within $3.5 < \eta < 5.09$ and that from particles within $-5.09 < \eta < -3.5$ from the AMPT model (with randomized reaction plane angle) for Au + Au collisions at 11.5A GeV. We see that $v_{1,\text{west}}\{\Psi_2\}$ is significantly anticorrelated with $v_{1,\text{east}}\{\Psi_2\}$. Figure 7(b) shows the event-by-event correlation between the reconstructed Ψ_1 and

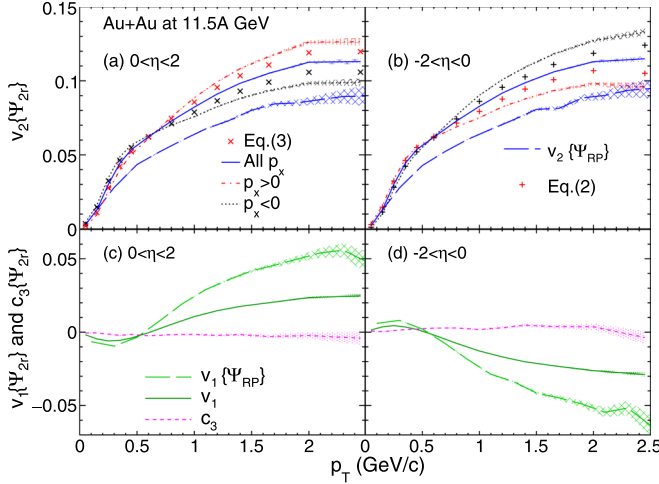


FIG. 8. Same as Fig. 5 for results after applying resolution corrections but relative to the event plane angle Ψ_{2r} .

Ψ_{2r} angles, which is strong and positive as expected. Therefore, we use Ψ_{2r} as the event plane angle for the v_2 splitting analysis in this section, where v_1 and v_2 are calculated using the two-subevent method [30]:

$$v_n^a\{\Psi_{2r}\} = \frac{\langle\langle \cos[n(\phi - \Psi_{2r}^b)] \rangle\rangle}{R_n^{\text{sub}}\{\Psi_{2r}^b\}}. \quad (8)$$

Note that c_3 is calculated similarly, and the two-subevent method removes the self-correlation between Ψ_{2r} and the flow coefficients (v_1 , v_2 , and c_3) calculated relative to Ψ_{2r} . The two subevents here are from $0 < \eta < 2$ and $-2 < \eta < 0$, and the subevent resolutions are calculated as $R_n^{\text{sub}}\{\Psi_{2r}\} = \sqrt{\langle \cos[n(\Psi_{2r}^a - \Psi_{2r}^b)] \rangle}$.

We show in Figs. 8(a) and 8(b) the v_2 splitting results of charged hadrons within $0 < \eta < 2$ and $-2 < \eta < 0$, respectively, after the resolution $R_2^{\text{sub}}\{\Psi_{2r}\}$ ($=0.433$ here) is applied. The overall $v_1\{\Psi_{2r}\}$ and $c_3\{\Psi_{2r}\}$ results are shown in Figs. 8(c) and 8(d), after the resolutions $R_1^{\text{sub}}\{\Psi_{2r}\}$ ($=0.715$ here) and $R_3^{\text{sub}}\{\Psi_{2r}\}$ ($=0.357$ here) are applied to correct v_1 and c_3 , respectively. The cross symbols and plus symbols represent respectively the expectations of Eq. (3) and Eq. (2) based on the corresponding overall corrected v_2 and v_1 . Similarly to Fig. 5, Eqs. (2) and (3) fail to describe the split v_2 curves, and this is due to the different resolution values. In addition, we see that although $v_2\{\Psi_{2r}\}$ are still higher than $v_2\{\Psi_{RP}\}$ (long-dashed curves in the upper panels), the difference between them is smaller than that between $v_2\{\Psi_1\}$ and $v_2\{\Psi_{RP}\}$. Furthermore, unlike $v_1\{\Psi_1\}$, $v_1\{\Psi_{2r}\}$ is much lower than $v_1\{\Psi_{RP}\}$ (long-dashed curves in the lower panels).

Figure 9 shows the raw results relative to Ψ_{2r} without resolution corrections. Similarly to the raw results relative to Ψ_1 shown in Fig. 6, the raw v_2 split curves relative to Ψ_{2r} also agree well with the expectations from Eqs. (2) and (3). As a result, the raw overall v_2 extracted with Eq. (3) from the split v_2 measurements relative to Ψ_{2r} can be corrected with its event plane resolution to yield the corrected v_2 , which will be equivalent to the standard $v_2\{\Psi_2\}$. Therefore, the v_2 splitting measurement should be feasible experimentally, using either

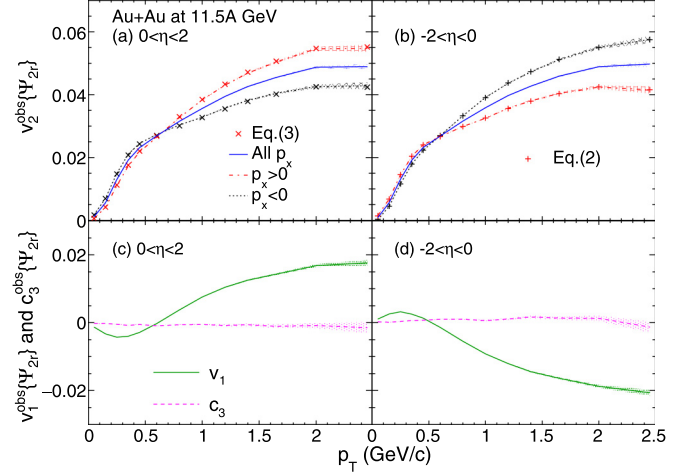


FIG. 9. Same as Fig. 6 for results without the resolution corrections but relative to the event plane angle Ψ_{2r} .

the first-order event plane Ψ_1 or the directional second-order event plane Ψ_{2r} .

Figure 10 shows in panel (a) the $v_2(p_x > 0)$ and $v_2(p_x < 0)$ results of charged hadrons within $0 < \eta < 2$ from the AMPT model for minimum bias Au + Au collisions at 11.5A GeV relative to three angles: the first-order event plane angle Ψ_1 , the directional second-order event plane angle Ψ_{2r} , and the theoretical reaction plane angle Ψ_{RP} . The corresponding results for the v_2 splitting, i.e., $v_2(p_x > 0) - v_2(p_x < 0)$, are shown in panel (b). We see in panel (a) that the $v_2(p_x > 0)$ and $v_2(p_x < 0)$ results (after applying the resolution correction) relative to the event plane angle Ψ_{2r} agree better with, although are somewhat higher than, the results relative to the reaction plane. From Fig. 10(b), it is clear that the v_2 splitting relative to the event plane angle Ψ_{2r} is much closer to that relative to the reaction plane. Therefore, the directional second-order event plane Ψ_{2r} is preferred from the perspective of measuring the v_2 splitting.

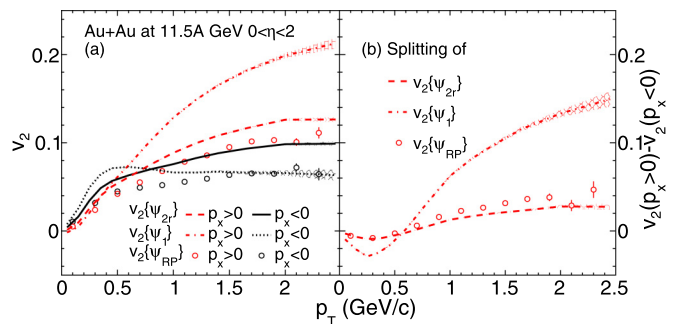


FIG. 10. (a) The split v_2 and (b) the v_2 splitting $v_2(p_x > 0) - v_2(p_x < 0)$ of charged hadrons within $0 < \eta < 2$ relative to the event plane angle Ψ_1 , Ψ_{2r} , and the theoretical reaction plane angle Ψ_{RP} (circles) as functions of the transverse momentum from the AMPT model for minimum bias Au + Au collisions at 11.5A GeV.

V. DISCUSSION

We emphasize that the string melting AMPT model currently cannot describe the directed flow well [32,33], even though the model typically well describes the elliptic and triangular flows. Therefore, results of the v_2 splitting from the AMPT model in this study are used primarily to demonstrate the relationship between the v_2 splitting and v_1 as shown in Eqs. (2) and (3). The AMPT results of $v_1(p_T)$ and the v_2 splitting here are not intended as quantitative predictions for the experimental observables; instead, they represent the exploration of the v_2 splitting possibilities. The inability of the string melting AMPT model to reproduce v_1 observables is related to its neglect of the finite (i.e., nonzero) nuclear thickness along the beam (z) direction, because the nuclear z width varies along the x direction and would thus affect the tilted shape of the created matter. In addition, the finite nuclear thickness has been shown to significantly affect the energy density of the dense matter at low energies [34,35] and the dynamics at finite rapidities even at high energies [36].

It has been realized in recent years that noncentral heavy ion collisions are affected by other interesting effects such as a strong electromagnetic field [37,38] and vorticity field [39]. For example, a significant fraction of the initial total angular momentum in a noncentral heavy ion collision is deposited into the created dense matter and thus creates a global vorticity field, which leads to global polarization of hyperons and spin alignment of vector mesons that have been observed [39–41]. Since we find that the left-right v_2 splitting is mostly due to v_1 , it will be interesting to study how the vorticity field affects the development of v_1 and consequently the v_2 splitting [17]. Note that the global vorticity field and v_1 share several similarities; e.g., the magnitude is usually larger at larger rapidities, and they both have a left-right antisymmetry.

More generally, it will be useful to study the correlations and relationships among anisotropic flows, the electromagnetic field, and the vorticity field. For example, the splitting of charm and anticharm directed flows has been proposed as a result of the electromagnetic field [42]. The rotation of the created matter has also been shown to affect the flow pattern, especially the directed flow [43]. The dynamics that generates v_1 is quite complicated, as v_1 depends on the equation of state, mean-field potentials, particle rescatterings, shadowing from spectator nucleons, and the tilt of the created matter in the x - z plane [44–46]. On the other hand, v_2 depends on the geometry of the created matter in the x - y plane. Therefore, the left-right v_2 splitting reflects the three-dimensional geometry and dynamical evolution of the dense matter.

VI. SUMMARY

We have examined the left-right splitting of the elliptic flow, on opposite sides of the impact parameter axis, that has been recently proposed as a new effect due to the global vorticity in noncentral heavy ion collisions. In this study, we find that this v_2 splitting is due to the nonzero directed flow v_1 at finite rapidities and approximately given by $8v_1(1 - 3v_2)/(3\pi)$. Therefore, the splitting is expected to depend sensitively on the transverse momentum, rapidity range, and particle species.

We also use the string melting version of a multiphase transport model, which automatically includes the vorticity field and flow fluctuations and usually describes well the elliptic and triangular flows. Our model results confirm the existence of the v_2 splitting at finite rapidities on both parton and hadron levels above certain transverse momenta. We also find that the relative splitting may be significant even for central heavy ion collisions, the splitting within a fixed (pseudo)rapidity range is expected to decrease with the colliding energy, and the splitting at large rapidity may be significant even at LHC energies. In addition, we find that the v_2 splitting should be measurable experimentally with the event plane method using either the first- or second-order event plane, and that the analytical expectations for the v_2 splitting apply to the raw v_2 and v_1 (i.e., before applying their respective event plane resolutions) in each case. Therefore, one can extract the raw overall v_1 and v_2 from the v_2 splitting measurements. In the typical case where $c_3 \simeq 0$, after applying event plane resolutions the corrected overall v_1 is equivalent to the usual v_1 if the v_2 splitting is measured relative to the first-order event plane, while the corrected overall v_2 is equivalent to the usual v_2 if the v_2 splitting is measured relative to the second-order event plane. From the perspective of measuring the split v_2 , the directional second-order event plane Ψ_{2r} is preferred since its v_2 results agree better with those relative to the reaction plane. The left-right v_2 splitting, as a complementary observable to the standard flow observables, will benefit the studies of the three-dimensional geometry and dynamical evolution of the dense matter created in heavy ion collisions.

ACKNOWLEDGMENTS

C.Z. acknowledges support from the Chinese Scholarship Council. This work is supported by the National Science Foundation under Grant No. 2012947 (Z.-W.L.).

-
- [1] E. V. Shuryak, *Phys. Lett. B* **78**, 150 (1978).
 - [2] S. Voloshin and Y. Zhang, *Z. Phys. C* **70**, 665 (1996).
 - [3] B. Alver and G. Roland, *Phys. Rev. C* **81**, 054905 (2010); **82**, 039903(E) (2010).
 - [4] K. H. Ackermann *et al.* (STAR Collaboration), *Phys. Rev. Lett.* **86**, 402 (2001).
 - [5] S. S. Adler *et al.* (PHENIX Collaboration), *Phys. Rev. Lett.* **91**, 182301 (2003).
 - [6] K. Aamodt *et al.* (ALICE Collaboration), *Phys. Rev. Lett.* **105**, 252302 (2010).
 - [7] C. Aidala *et al.* (PHENIX Collaboration), *Nat. Phys.* **15**, 214 (2019).
 - [8] S. Chatrchyan *et al.* (CMS Collaboration), *Phys. Lett. B* **724**, 213 (2013).
 - [9] K. Dusling, M. Mace, and R. Venugopalan, *Phys. Rev. Lett.* **120**, 042002 (2018).

- [10] M. Mace, V. V. Skokov, P. Tribedy, and R. Venugopalan, *Phys. Rev. Lett.* **121**, 052301 (2018); **123**, 039901(E) (2019).
- [11] L. He, T. Edmonds, Z.-W. Lin, F. Liu, D. Molnar, and F. Wang, *Phys. Lett. B* **753**, 506 (2016).
- [12] Z.-W. Lin, L. He, T. Edmonds, F. Liu, D. Molnar, and F. Wang, *Nucl. Phys. A* **956**, 316 (2016).
- [13] A. Kurkela, U. A. Wiedemann, and B. Wu, *Phys. Lett. B* **783**, 274 (2018).
- [14] A. Kurkela, U. A. Wiedemann, and B. Wu, *Eur. Phys. J. C* **79**, 965 (2019).
- [15] R. D. Weller and P. Romatschke, *Phys. Lett. B* **774**, 351 (2017).
- [16] U. W. Heinz and J. S. Moreland, *J. Phys.: Conf. Ser.* **1271**, 012018 (2019).
- [17] Z. Chen, Z. Wang, C. Greiner, and Z. Xu, [arXiv:2108.12735](https://arxiv.org/abs/2108.12735).
- [18] Z.-W. Lin, C. M. Ko, B.-A. Li, B. Zhang, and S. Pal, *Phys. Rev. C* **72**, 064901 (2005).
- [19] C. Zhang, L. Zheng, S. Shi, and Z.-W. Lin, *Phys. Rev. C* **104**, 014908 (2021).
- [20] Z.-W. Lin and C. M. Ko, *Phys. Rev. C* **65**, 034904 (2002).
- [21] G.-L. Ma and Z.-W. Lin, *Phys. Rev. C* **93**, 054911 (2016).
- [22] Y. Jiang, Z.-W. Lin, and J. Liao, *Phys. Rev. C* **94**, 044910 (2016); **95**, 049904(E) (2017).
- [23] H. Li, L.-G. Pang, Q. Wang, and X.-L. Xia, *Phys. Rev. C* **96**, 054908 (2017).
- [24] Y. He and Z.-W. Lin, *Phys. Rev. C* **96**, 014910 (2017).
- [25] C. Zhang, L. Zheng, F. Liu, S. Shi, and Z.-W. Lin, *Phys. Rev. C* **99**, 064906 (2019).
- [26] L. Zheng, C. Zhang, S. S. Shi, and Z.-W. Lin, *Phys. Rev. C* **101**, 034905 (2020).
- [27] J. Xu, L.-W. Chen, C. M. Ko, and Z.-W. Lin, *Phys. Rev. C* **85**, 041901(R) (2012).
- [28] J. Xu, T. Song, C. M. Ko, and F. Li, *Phys. Rev. Lett.* **112**, 012301 (2014).
- [29] A. M. Poskanzer and S. A. Voloshin, *Phys. Rev. C* **58**, 1671 (1998).
- [30] S. A. Voloshin, A. M. Poskanzer, and R. Snellings, *Landolt-Bornstein* **23**, 293 (2010).
- [31] J. Adams *et al.*, *Nucl. Instrum. Methods Phys. Res., Sect. A* **968**, 163970 (2020).
- [32] K. Nayak, S. Shi, N. Xu, and Z.-W. Lin, *Phys. Rev. C* **100**, 054903 (2019).
- [33] K. Nayak (STAR Collaboration), *Nucl. Phys. A* **1005**, 121855 (2021).
- [34] Z.-W. Lin, *Phys. Rev. C* **98**, 034908 (2018).
- [35] T. Mendenhall and Z.-W. Lin, *Phys. Rev. C* **103**, 024907 (2021).
- [36] C. Shen and B. Schenke, *Phys. Rev. C* **97**, 024907 (2018).
- [37] V. Voronyuk, V. D. Toneev, W. Cassing, E. L. Bratkovskaya, V. P. Konchakovski, and S. A. Voloshin, *Phys. Rev. C* **83**, 054911 (2011).
- [38] W.-T. Deng and X.-G. Huang, *Phys. Rev. C* **85**, 044907 (2012).
- [39] L. Adamczyk *et al.* (STAR Collaboration), *Nature (London)* **548**, 62 (2017).
- [40] Z.-T. Liang and X.-N. Wang, *Phys. Rev. Lett.* **94**, 102301 (2005); **96**, 039901(E) (2006).
- [41] S. Acharya *et al.* (ALICE Collaboration), *Phys. Rev. Lett.* **125**, 012301 (2020).
- [42] S. K. Das, S. Plumari, S. Chatterjee, J. Alam, F. Scardina, and V. Greco, *Phys. Lett. B* **768**, 260 (2017).
- [43] L. P. Csernai, D. D. Strottman, and C. Anderlik, *Phys. Rev. C* **85**, 054901 (2012).
- [44] R. J. M. Snellings, H. Sorge, S. A. Voloshin, F. Q. Wang, and N. Xu, *Phys. Rev. Lett.* **84**, 2803 (2000).
- [45] C. Zhang, J. Chen, X. Luo, F. Liu, and Y. Nara, *Phys. Rev. C* **97**, 064913 (2018).
- [46] Y. Nara, H. Niemi, A. Ohnishi, and H. Stöcker, *Phys. Rev. C* **94**, 034906 (2016).